

Effect of nonresonant states in near-resonant two-photon ionization of hydrogenXu Zhang ¹, Yueming Zhou ^{1,*}, Yijie Liao,¹ Yongkun Chen,¹ Jintai Liang,¹ Qinghua Ke,¹ Min Li,¹ András Csehi ^{2,†} and Peixiang Lu^{1,3}¹*School of Physics and Wuhan National Laboratory for Optoelectronics, Huazhong University of Science and Technology, Wuhan 430074, China*²*Department of Theoretical Physics, Faculty of Science and Technology, University of Debrecen, PO Box 400, H-4002 Debrecen, Hungary*³*Optics Valley Laboratory, Hubei 430074, China*

(Received 1 September 2022; accepted 20 December 2022; published 30 December 2022)

By numerically solving the three-dimensional time-dependent Schrödinger equation, two-photon ionization of hydrogen is investigated at the near-resonant frequencies of the $1s$ - $2p$ transition. Due to the Rabi oscillations between the $1s$ and $2p$ states, the photoelectron energy spectra exhibit the Autler-Townes (AT) doublets and we focus on the energy spacing and the asymmetry of the doublets. Our results show that the laser frequency for the minimum energy spacing of AT doublets locates at the resonant frequency of the ac-stark-shifted states, while the symmetry of the AT doublets is affected both by the ac-stark shift and the nonresonant ionization pathway. Developing the minimal three-state model including all of the nonresonant (nonessential) states, the effects of the ac-stark shift and the nonresonant ionization pathway on the AT doublets due to the nonresonant states are identified. Furthermore, due to the nonresonant ionization pathway, the photoelectron angular distributions are distinctly different for the lower- and higher-energy peaks in the AT doublets and these angular distributions sensitively depend on the laser intensity and pulse duration. These results are well reproduced by our minimal three-state model.

DOI: [10.1103/PhysRevA.106.063114](https://doi.org/10.1103/PhysRevA.106.063114)**I. INTRODUCTION**

Photoionization is a fundamental process in the light-matter interaction. It has been extensively studied since the advent of quantum mechanics. The development of new laser sources during the last decades, such as high-harmonic generation and free electron lasers [1–4], has enabled the two-photon ionization (TPI) and multiphoton ionization (MPI) [5–7]. The resonance in TPI and MPI has attracted intensive interest and Rabi oscillations are the prominent features of resonant TPI and MPI [8–17].

Rabi oscillations are periodic population transitions between the dressed initial and resonant states induced by a time-varying field, which result in Autler-Townes (AT) splittings in the photoelectron energy spectra [18–23]. The energy spacing between the splittings equals the Rabi frequency [10] $\Omega = eE_0D_{IR}/\hbar$ (E_0 , D_{IR} , \hbar , and e are the electric-field amplitude, the transition dipole between the initial and resonant states, the reduced Planck constant, and the elementary charge, respectively). Recently, Rabi oscillations were observed with intense coherent laser pulses [24–26]. The Rabi dynamics can be well described in the basis of Floquet states [27–29]. The concept of the Floquet states (dressed states) is used to be applied in monochromatic laser field. However, for the laser pulses with very short duration, the pulse envelope has a significant impact on the photoionization

and is important to be taken into consideration [30–32]. For example, the envelope of the laser pulse could induce the dynamic interference of photoelectrons in photonization by the high-frequency laser [31,33–43].

In recent years, numerous studies related to resonant TPI and MPI were reported. For instance, it was shown that the ionization probability deviates obviously from the conventional I^n scaling when Rabi oscillations occur [25,44,45]. The Rabi frequency in the resonant three-photon ionization process of potassium atoms was experimentally surveyed with an 800-nm femtosecond laser [17], and it was shown that the measured result agrees well with the effective Rabi frequency, which takes into account the ionization process [46]. The majority of the previous studies focused on the relatively low laser intensities and thus only the resonant photoionization pathway dominates. However, as the laser intensity increases, the impacts of the nonresonant states become more important and it is necessary to take into account the effects of these states. It was shown that, in the TPI process at the near-resonant frequencies, the nonresonant pathway through the nonresonant states is significant at the high-laser intensities. The competition between the resonant and the nonresonant pathways affects the photoelectron angular distribution (PAD) [47,48]. Additionally, the influence of the ac-stark shift arising from nonresonant states on the energy splitting and the asymmetry of the AT doublets was theoretically demonstrated [43].

Very recently, with the seeded free-electron laser in the extreme ultraviolet (XUV) frequency regime, resonant TPI of He was studied and the AT doublet in the energy spectra

*zhouymhust@hust.edu.cn

†csehi.andras@science.unideb.hu

was observed [49]. It was shown that the doublets were asymmetric at such high-laser intensity. Theoretical calculations proved that, due to the intermediate nonresonant states in the two-photon transition, the nonresonant TPI possesses a giant effective dipole moment, which resulted in the comparable contributions of the two-photon ionization from the ground state (the nonresonant pathway) and the one-photon ionization pathway from the excited state (the resonant pathway). The interference of the resonant and nonresonant TPI pathways gave rise to the asymmetric doublets in the photoelectron energy spectrum.

In this work, we demonstrate the effects of the nonresonant states in near-resonant TPI at high-laser intensities from two aspects. One is the ac-stark shifts of the initial, the resonant, and the continuum states and the other is the nonresonant TPI pathway from the initial state. We study the TPI of hydrogen by solving the three-dimensional time-dependent Schrödinger equation (3D-TDSE) at the near-resonant frequencies. The obtained photoelectron spectra (PESs) show that the laser frequency where the minimum energy spacing of AT doublets locates and the laser frequency where the symmetric AT doublets appears are both blue shifted from the field-free resonant frequency of 0.375 a.u. Moreover, the laser frequency for the symmetric AT doublets is both laser-intensity and pulse-duration dependent, while the frequency for the minimum energy spacing of AT doublets depends on laser intensity but not on the pulse duration. Furthermore, the photoelectron angular distributions (PADs) are distinctly different for the lower- and higher-energy peaks of the AT doublets and these angular distributions sensitively depend on both the laser intensity and pulse duration. To understand the above phenomena, a minimal three-state model which takes into account all the nonresonant states as well as the pulse envelope is developed. Both the PESs and the photo-electron momentum distributions (PEMDs) from this model are in good agreement with the TDSE results. Based on this agreement, the effects of the ac-stark shifts and the nonresonant ionization pathway due to the nonresonant states are identified.

II. METHODS

A. Numerically solving the TDSE

The PEMDs are obtained by numerically solving the 3D-TDSE of the hydrogen atomic system in a velocity gauge. In this paper, atomic units (a.u.) are used unless otherwise noted.

TDSE is written as

$$i \frac{\partial \psi(\mathbf{r}, t)}{\partial t} = H(\mathbf{r}, t) \psi(\mathbf{r}, t), \quad (1)$$

where

$$H(\mathbf{r}, t) = -\frac{1}{2} \nabla^2 - \frac{1}{r} - i \mathbf{A}(t) \cdot \nabla. \quad (2)$$

∇ is the gradient operator, $\mathbf{A}(t)$ is the vector potential of laser field in the dipole approximation, it is written as

$$\mathbf{A}(t) = A_0 \sin^2 \left(\frac{\omega t}{2N} \right) \sin(\omega t) \mathbf{e}_y, \quad (3)$$

where A_0 is the amplitude of the vector potential, ω is the angular frequency of laser field, and N is the number of the optical cycles.

The 3D-TDSE in Eq. (1) is solved in the spherical coordinates, where the wave function $\psi(\mathbf{r}, t)$ is expanded by the spherical harmonics $|l, m\rangle$

$$|\psi(\mathbf{r}, t)\rangle = \sum_{l, m} \frac{R_{lm}(r, t)}{r} |l, m\rangle. \quad (4)$$

Here, $R_{lm}(r, t)$ is the radial part of the wave function, which is discretized by the finite-element discrete variable representation method [50]. The time propagation of the TDSE is calculated by the split-Lanczos [51] method with the time step of $\Delta t = 0.01$ a.u.

The initial wave function is chosen as the $1s$ state here which is prepared by imaginary-time propagation. During the propagation of the wave function, we split the wave function $\psi(\mathbf{r}, t)$ into $\psi_{in}(\mathbf{r}, t)$ and $\psi_{out}(\mathbf{r}, t)$ at some time points during the TDSE calculations, $\psi_{in}(\mathbf{r}, t) = \psi(\mathbf{r}, t) F_{sp}$ and $\psi_{out}(\mathbf{r}, t) = \psi(\mathbf{r}, t) (1 - F_{sp})$. F_{sp} is the absorbing mask function which reads $F_{sp} = 1 - (1 + e^{(R-R_c)/d})^{-1}$. $\psi_{in}(\mathbf{r}, t)$ is evolved as TDSE, and $\psi_{out}(\mathbf{r}, t)$ is propagated by the Coulomb-Volkov propagator [52] and then projected to the scattering state $\langle \psi_{\mathbf{k}}(\mathbf{r}) | \psi_{out}(\mathbf{r}, t) \rangle$ to obtain the ionization amplitudes.

In our numerical simulations, the maximal box size R_{max} for radial coordinates is $R_{max} = 2000$ a.u. The absorbing boundary R_c is 1600 a.u., $d = 2$ a.u.. The number of partial waves in Eq. (4) is chosen to be $L_{max} = 10$, which ensures convergence of the calculations.

B. Minimal three-state model

The time-dependent wave function can be expanded as

$$|\Psi\rangle = a_I(t) e^{-iE_I t} |I\rangle + a_R(t) e^{-iE_R t} |R\rangle + \sum_n \int d\varepsilon a_n(t) e^{-iE_n t} |n\rangle + \int d\varepsilon a_\varepsilon(t) e^{-iE_\varepsilon t} |\varepsilon\rangle, \quad (5)$$

where $|I\rangle$ and $|R\rangle$ represent the initial and the resonant states, respectively. $|\varepsilon\rangle$ represents the continuum states and all the nonresonant states are labeled by $|n\rangle$.

Inserting Eq. (5) into Eq. (1) in the length gauge [$H(\mathbf{r}, t) = -\frac{1}{2} \nabla^2 - \frac{1}{r} + \mathbf{r} \cdot \mathbf{E}(t)$], we obtain the four-state model

$$\begin{aligned} i \dot{a}_I(t) &= D_{IR} \frac{1}{2} E_0 g(t) e^{i\Delta\omega t} a_R(t) + D_{IR} \frac{1}{2} E_0 g(t) e^{i(-\omega - E_R + E_I)t} a_R(t) \\ &+ \sum_n \int D_{In} \frac{1}{2} E_0 g(t) e^{i(E_I - E_n + \omega)t} a_n(t) + \sum_n \int D_{In} \frac{1}{2} E_0 g(t) e^{i(E_I - E_n - \omega)t} a_n(t), \end{aligned} \quad (6a)$$

$$\begin{aligned}
i\dot{a}_R(t) &= D_{RI} \frac{1}{2} E_0 g(t) e^{-i\Delta\omega t} a_I(t) + D_{RI} \frac{1}{2} E_0 g(t) e^{-i(-\omega - E_R + E_I)t} a_I(t) \\
&+ \int d\varepsilon D_{R\varepsilon} \frac{1}{2} E_0 g(t) e^{i(E_R - E_\varepsilon + \omega)t} a_\varepsilon(t) + \int d\varepsilon D_{R\varepsilon} \frac{1}{2} E_0 g(t) e^{i(E_R - E_\varepsilon - \omega)t} a_\varepsilon(t) \\
&+ \sum_n^f D_{Rn} \frac{1}{2} E_0 g(t) e^{i(E_R - E_n + \omega)t} a_n(t) + \sum_n^f D_{Rn} \frac{1}{2} E_0 g(t) e^{i(E_R - E_n - \omega)t} a_n(t), \quad (6b)
\end{aligned}$$

$$\begin{aligned}
i\dot{a}_n(t) &= D_{nI} \frac{1}{2} E_0 g(t) e^{-i(E_I - E_n + \omega)t} a_I(t) + D_{nI} \frac{1}{2} E_0 g(t) e^{-i(E_I - E_n - \omega)t} a_I(t) \\
&+ D_{nR} \frac{1}{2} E_0 g(t) e^{-i(E_R - E_n + \omega)t} a_R(t) + D_{nR} \frac{1}{2} E_0 g(t) e^{-i(E_R - E_n - \omega)t} a_R(t) \\
&+ \int d\varepsilon D_{n\varepsilon} \frac{1}{2} E_0 g(t) e^{i(E_n - E_\varepsilon + \omega)t} a_\varepsilon(t) + \int d\varepsilon D_{n\varepsilon} \frac{1}{2} E_0 g(t) e^{i(E_n - E_\varepsilon - \omega)t} a_\varepsilon(t), \quad (6c)
\end{aligned}$$

$$\begin{aligned}
i\dot{a}_\varepsilon(t) &= D_{\varepsilon R} \frac{1}{2} E_0 g(t) e^{-i(E_R - E_\varepsilon + \omega)t} a_R(t) + D_{\varepsilon R} \frac{1}{2} E_0 g(t) e^{-i(E_R - E_\varepsilon - \omega)t} a_R(t) \\
&+ \sum_n^f D_{\varepsilon n} \frac{1}{2} E_0 g(t) e^{-i(E_n - E_\varepsilon + \omega)t} a_n(t) + \sum_n^f D_{\varepsilon n} \frac{1}{2} E_0 g(t) e^{-i(E_n - E_\varepsilon - \omega)t} a_n(t). \quad (6d)
\end{aligned}$$

Here $\Delta\omega = \omega - \omega_{RI}$ ($\omega_{ij} = E_i - E_j$) is the energy detuning, $D_{IR} = \langle I|\hat{z}|R\rangle$, $D_{R\varepsilon} = \langle R|\hat{z}|\varepsilon\rangle$, $D_{nI} = \langle n|\hat{z}|I\rangle$, $D_{nR} = \langle n|\hat{z}|R\rangle$, and $D_{n\varepsilon} = \langle n|\hat{z}|\varepsilon\rangle$ are defined as the transition dipole matrix element between the initial and resonant states, the resonant and the continuum states, nonresonant and initial states, nonresonant and resonant states, and nonresonant and continuum states, respectively.

As the nonresonant states are far from resonance, they are not significantly populated during the interaction with the laser field. The amplitudes of these states can be adiabatically eliminated [53]. After integrating Eq. (6c) by parts and omitting small terms [the $g(t)$ envelope function evolves much slower than the $T_0 = 2\pi/\omega$ time period of the laser], we obtain the expression for $a_n(t)$

$$\begin{aligned}
a_n(t) &= D_{nI} \frac{1}{2} E_0 g(t) \frac{e^{-i(E_I - E_n + \omega)t}}{E_I - E_n + \omega} a_I(t) + D_{nI} \frac{1}{2} E_0 g(t) \frac{e^{-i(E_I - E_n - \omega)t}}{E_I - E_n - \omega} a_I(t) \\
&+ D_{nR} \frac{1}{2} E_0 g(t) \frac{e^{-i(E_R - E_n + \omega)t}}{E_R - E_n + \omega} a_R(t) + D_{nR} \frac{1}{2} E_0 g(t) \frac{e^{-i(E_R - E_n - \omega)t}}{E_R - E_n - \omega} a_R(t) \\
&+ \int d\varepsilon D_{n\varepsilon} \frac{1}{2} E_0 g(t) \frac{e^{-i(E_\varepsilon - E_n - \omega)t}}{E_\varepsilon - E_n - \omega} a_\varepsilon(t) + \int d\varepsilon D_{n\varepsilon} \frac{1}{2} E_0 g(t) \frac{e^{-i(E_\varepsilon - E_n + \omega)t}}{E_\varepsilon - E_n + \omega} a_\varepsilon(t). \quad (7)
\end{aligned}$$

Inserting Eq. (7) into the coupled differential equations Eq. (6), the four-state model is simplified to the three-state model. Then, the three-state model is further simplified by using the rotating wave approximation [54] to remove the rapidly oscillating components. Finally, applying the local approximation [55,56]

$$\begin{aligned}
\int d\varepsilon D_{R\varepsilon} \frac{1}{2} E_0 g(t) e^{i\delta t} a_\varepsilon(t) &= -\frac{i}{2} \Gamma_R(t) a_R(t), \\
\int d\varepsilon \tilde{M}_{I\varepsilon} \left(\frac{1}{2} E_0 g(t) \right)^2 e^{i\delta_I t} a_\varepsilon(t) &= -\frac{i}{2} \Gamma_I(t) a_I(t), \quad (8)
\end{aligned}$$

we obtain the minimal three-state model as

$$i\dot{a}_I(t) = \left[S_I(t) - \frac{i}{2} \Gamma_I(t) \right] a_I(t) + D_{IR} \frac{1}{2} E_0 g(t) e^{i\Delta\omega t} a_R(t), \quad (\text{I})$$

$$i\dot{a}_R(t) = D_{IR} \frac{1}{2} E_0 g(t) e^{-i\Delta\omega t} a_I(t) + \left[S_R(t) - \frac{i}{2} \Gamma_R(t) \right] a_R(t), \quad (\text{II})$$

$$i\dot{a}_\varepsilon(t) = \tilde{M}_{I\varepsilon}^\dagger \left(\frac{1}{2} E_0 g(t) \right)^2 e^{-i\delta_I t} a_I(t) + D_{R\varepsilon} \frac{1}{2} E_0 g(t) e^{-i\delta t} a_R(t) + S_\varepsilon(t) a_\varepsilon(t). \quad (\text{III}) \quad (9)$$

Here,

$$\delta = E_R - E_\varepsilon + \omega, \quad \delta_I = E_I - E_\varepsilon + 2\omega, \quad (10a)$$

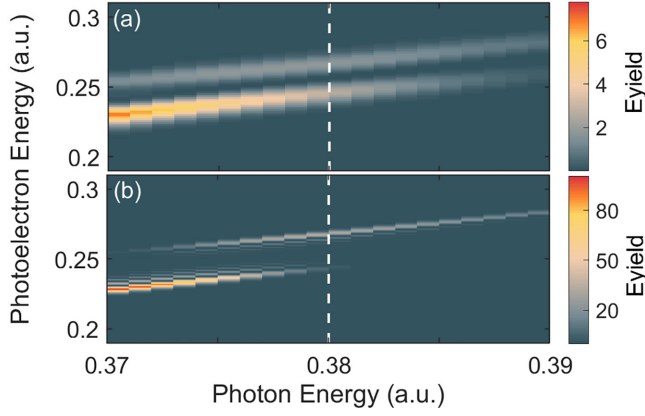


FIG. 1. The PES as a function of the laser frequency obtained from the 3D-TDSE. The laser intensity is $I = 5 \times 10^{13}$ W/cm² and the pulse durations are $N = 60, 300$ for (a), (b), respectively. In each case, the dashed white line corresponds to the photon energy for the minimum energy spacing of the AT doublet.

are the energy detunings and

$$\tilde{M}_{I\varepsilon} = \sum_{n \neq I, \neq R} \frac{\langle I|z|n\rangle \langle n|z|\varepsilon\rangle}{E_\varepsilon - E_n - \omega} \quad (10b)$$

is the two-photon transition matrix element from the dressed initial state to the continuum state through the nonresonant states where

$$\begin{aligned} S_\varepsilon(t) &= U_p(t), \\ S_I(t) &= \sum_{n \neq I, \neq R} \left(D_{In} \frac{1}{2} E_0 g(t) \right)^2 \frac{2\omega_{In}}{\omega_{In}^2 - \omega^2} = S_{I0} E_0^2 g^2(t), \\ S_R(t) &= \sum_{n \neq I, \neq R} \left(D_{Rn} \frac{1}{2} E_0 g(t) \right)^2 \frac{2\omega_{Rn}}{\omega_{Rn}^2 - \omega^2} = S_{R0} E_0^2 g^2(t), \end{aligned} \quad (10c)$$

are the dynamic stark shifts of the continuum, initial, and resonant states, respectively. The stark shift for the continuum state approximately equals to the time-dependent ponderomotive shift $U_p(t) = \frac{E_0^2}{4\omega^2} g^2(t)$ where

$$\begin{aligned} \Gamma_R(t) &= 2\pi |D_{R\varepsilon}|^2 \left(\frac{1}{2} E_0 g(t) \right)^2, \\ \Gamma_I(t) &= 2\pi |\tilde{M}_{I\varepsilon}|^2 \left(\frac{1}{2} E_0 g(t) \right)^4, \end{aligned} \quad (10d)$$

represent the ionization rates from the resonant state $|R\rangle$ and the initial state $|I\rangle$, respectively. $\Gamma_R(t)$ and $\Gamma_I(t)$ denote the resonant and the nonresonant ionization pathways, respectively.

III. NUMERICAL RESULTS AND DISCUSSIONS

A. Energy splitting and asymmetry of the AT doublets in PES

Figure 1 shows the photoelectron spectra as a function of the laser frequency varying from 0.370 to 0.390 a.u., where the laser intensity is 5×10^{13} W/cm². The pulse durations are $N = 60$ (full width at half maximum, FWHM $\cong 12$ fs) and $N = 300$ (FWHM $\cong 60$ fs) for Figs. 1(a) and 1(b), respectively. The Autler-Townes splitting of the energy spectra is

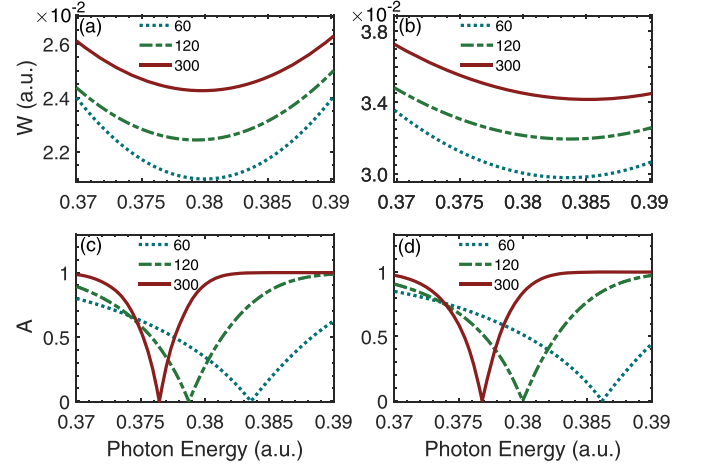


FIG. 2. (a), (b) The energy spacing of the doublets (W) as a function of the laser frequency. (c), (d) The asymmetry of the doublets (A) as a function of the laser frequency. The laser intensities are 5×10^{13} W/cm² in (a) and (c), and 1×10^{14} W/cm² in (b), (d). The blue dotted, green dashed, and red solid lines represent the results from TDSE with the pulse durations $N = 60, 120$, and 300 , respectively.

clearly seen, which is a manifest of Rabi oscillations [8–17]. The sketch of the Autler-Townes splitting as a result of Rabi oscillations will be explained below (as shown in Fig. 7). The weak peaks between the doublets are due to the dynamic interference [31,33–43]. It is shown that the energy spacing of the AT doublets decreases first and then gradually increases with the laser frequency. This is more clearly seen in Fig. 2(a). The heights of the doublets are obviously asymmetric. The height of the higher-energy peak increases gradually as the laser frequency increases, while that of the lower-energy peak decreases gradually.

To quantitatively analyze the energy splitting and the asymmetry of the doublets, we plot the energy spacing W and the asymmetry A of doublets as a function of the laser frequency, as shown in Fig. 2. Here, the asymmetry A is defined as $A = \frac{|S_L - S_H|}{S_>}$, where S_L and S_H are the heights of the lower- and higher-energy peaks in the doublets, respectively. $S_>$ is the larger one of S_L and S_H . The laser intensities are 5×10^{13} W/cm² and 1×10^{14} W/cm² in Figs. 2(a) and 2(c) and Figs. 2(b) and 2(d), respectively.

At the low-laser intensity region, the resonant ionization pathway dominates. Previous studies on the near-resonant TPI were mostly focused on the lower laser intensity region [36,57]. In that case, the minimum energy spacing of the AT doublet occurs at the field-free resonant frequency (0.375 a.u. for H), where the doublets are symmetric. However, as the laser intensity increases, the effect of the nonresonant states emerges and the contribution of the nonresonant TPI pathway becomes visible. As shown in Figs. 2(a) and 2(b), the frequency ω_m^w for the minimum energy spacing no longer occurs at 0.375 a.u. At 5×10^{13} W/cm² and 1×10^{14} W/cm², it is located at 0.380 a.u. and 0.384 a.u., respectively. The value of the energy spacing increases with the pulse duration, but the frequency ω_m^w is independent on the pulse duration. For the asymmetry of doublets A , as shown in Figs. 2(c) and 2(d), the

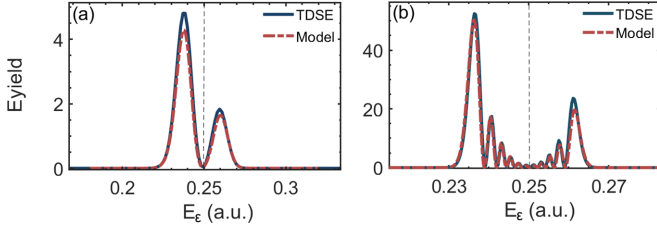


FIG. 3. The PES at the laser frequency $\omega = 0.375$ a.u. obtained from the minimal three-state model (red dashed lines) and TDSE (blue solid lines). The laser intensity is 5×10^{13} W/cm², and the pulse durations are $N = 60$ and 300 in (a), (b), respectively. The black dashed lines denote the expected kinetic energy (0.25 a.u.) of a photoelectron absorbing two resonant photons.

frequency ω_m^A that minimizes A is blue shifted compared to the field-free resonant frequency 0.375 a.u. This is consistent with the recent experiment on TPI of He [49]. The amount of the blue shift depends on the laser intensity and pulse duration. The shift is larger for the shorter pulse duration and stronger intensity.

These features are ascribed to the contribution of the nonresonant states. To understand the role of the nonresonant states, we resort to the minimal three-state model described in Sec. II (B) [Eq. (9)]. The PESs calculated by our minimal three-state model are shown in Fig. 3. The results from our model are calculated with optimized parameter values that $\tilde{M}_{I\varepsilon} = -7.5$ a.u., $S_{R0} = 2.6$ a.u., and $S_{I0} = -0.7$ a.u.. The optimized parameter values are calculated by comparing the PESs obtained from the three-state model [Eq. (9)] to the TDSE result at a given laser intensity, and could reproduce the TDSE results at other laser intensities. The agreement between the TDSE result and our model is excellent and it enables us to quantitatively analyze the effect of the nonresonant states.

As revealed in our model [Eq. (9)], the nonresonant states contribute in two ways. One is the ac-stark shifts of the initial, the resonant, and the continuum states, which are denoted as S_I , S_R , and S_ε , respectively. The other is the nonresonant ionization pathway denoted as $\tilde{M}_{I\varepsilon}$. To separately investigate these two effects of the nonresonant states, we first consider only the ac-stark shifts by setting $\tilde{M}_{I\varepsilon} = 0$ (i.e., with the non-

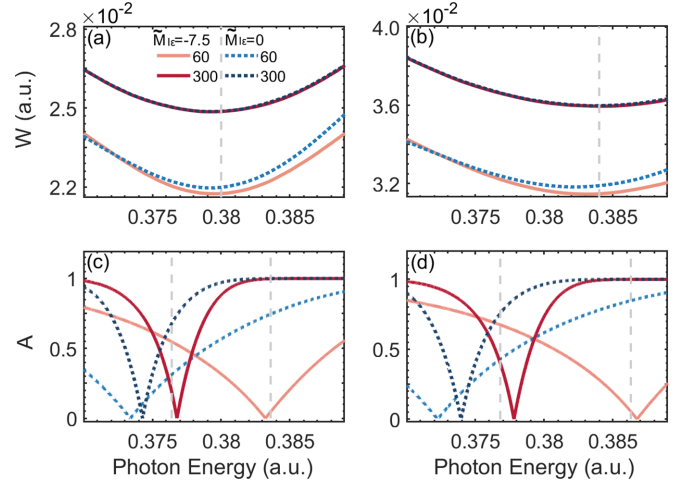


FIG. 4. (a), (b) The energy spacing of the doublets (W) as a function of the laser frequency obtained from the minimal three-state model. (c), (d) The asymmetry of the doublets (A) as a function of the laser frequency obtained from the minimal three-state model. The laser intensities are 5×10^{13} W/cm² and 1×10^{14} W/cm² in (a), (c) and (b), (d), respectively. The solid and dotted lines represent the results calculated from the minimal three-state model with $\tilde{M}_{I\varepsilon} = -7.5$ a.u. and $\tilde{M}_{I\varepsilon} = 0$ a.u., respectively. In each case, the gray dashed line corresponds to the frequency ω_m^A or ω_m^W obtained from TDSE (as shown in Fig. 2).

resonant ionization pathway being excluded), as indicated by the dotted blue lines in Fig. 4. Compared with the field-free resonant frequency 0.375 a.u., the frequency ω_m^W is larger than 0.375 a.u. and the frequency ω_m^A is smaller than 0.375 a.u.. To illustrate this, we diagonalize the Hamiltonian of Eq. (9) I and II ($\tilde{M}_{I\varepsilon} = 0$) to obtain the time-dependent eigenenergy and eigenstates, then the expressions for the effective Rabi frequency $\tilde{\Omega}$ (i.e., the energy spacing W) and the amplitude of the populated continuum state $a_\varepsilon(t)$ can be written as

$$\tilde{\Omega}(t) \cong \sqrt{[D_{IR}E_0g(t)]^2 + \left(\Delta\omega + S_I(t) - S_R(t) - \frac{i}{2}\Gamma_R(t)\right)^2} \quad (11)$$

$$a_\varepsilon(t) \cong \frac{1}{i} \int_0^T dt \{\Upsilon_+ e^{i\varepsilon t} - \Upsilon_- e^{i\varepsilon t}\}, \quad (12)$$

where

$$\Upsilon_\pm \cong \frac{D_{\varepsilon R} D_{RI} [\frac{1}{2} E_0 g(t)]^2}{\sqrt{2} \sqrt{[D_{RI} E_0 g(t)]^2 + [\Delta\omega + S_I(t) - S_R(t)]^2}} \times \sqrt{1 + \left(\frac{-\frac{1}{2}[\Delta\omega + S_I(t) - S_R(t)] \pm \frac{1}{2} \sqrt{[D_{RI} E_0 g(t)]^2 + [\Delta\omega + S_I(t) - S_R(t)]^2}}{D_{RI} [\frac{1}{2} E_0 g(t)]}\right)^2} \quad (13)$$

and

$$\varepsilon_\pm \cong E_\varepsilon - E_I - 2\omega + \frac{1}{2}\Delta\omega + S_\varepsilon(t) - \frac{1}{2}[S_R(t) + S_I(t)] \mp \frac{1}{2}\tilde{\Omega}(t). \quad (14)$$

As shown in Eq. (11), the minimum energy spacing (i.e., line W has a minimum) locates at the frequency ω_m^W where $(\Delta\omega + S_I(t) - S_R(t) - \frac{i}{2}\Gamma_R(t))^2$ has a minimum. Moreover, as shown in Eq. (12), the symmetric doublets (i.e., line A

has a minimum) locates at the frequency ω_m^A where $\Upsilon_+ = \Upsilon_-$ and $|\varepsilon_+| = |\varepsilon_-|$. Therefore, the frequency ω_m^w is only related to $S_R(t) - S_I(t)$ [Eq. (11)], whereas the frequency ω_m^A is related to both $S_R(t) - S_I(t)$ and $S_R(t) + S_I(t) - 2S_\varepsilon(t)$ which are reflected in the prefactors Υ_\pm and the index factors ε_\pm , respectively [Eq. (13) and (14)]. Due to the frequency ω_m^w and ω_m^A being differently affected by the ac-stark shifts, they shift differently from the field-free resonant frequency 0.375 a.u.

Next, we reveal how the nonresonant ionization pathway affects the PES. We obtain the PES from the minimal three-state model with the nonresonant ionization pathway included ($\tilde{M}_{I\varepsilon} = -7.5$ a.u.). The results are shown by the solid lines in Fig. 4. The energy spacing W of the AT doublets obtained with $\tilde{M}_{I\varepsilon} = -7.5$ a.u. and $\tilde{M}_{I\varepsilon} = 0$ a.u. are almost the same. This is due to the fact that the energy splitting is only related to the energy shifts, not affected by contribution of the nonresonant ionization pathway. For the asymmetry A of the doublets, due to the effect of $\tilde{M}_{I\varepsilon}$, the frequency ω_m^A is significantly right-shifted, which is consistent with TDSE results. In conclusion, both the nonresonant ionization pathway and the ac-stark shifts arising from the nonresonant states affect the asymmetry of the doublets, but the contribution of the nonresonant ionization pathway dominates. For this reason, a slight blue-shift is always required to obtain symmetric doublets in the experiment.

In terms of the laser intensity dependence of the frequencies ω_m^w and ω_m^A , we note that both the frequencies ω_m^w and ω_m^A move further away from 0.375 a.u. as the laser intensity increases, regardless of whether the nonresonant ionization pathway $\tilde{M}_{I\varepsilon}$ is included or not. It is because the parameters S_I , S_R , S_ε , and $\tilde{M}_{I\varepsilon}$ that determine the location of ω_m^w and ω_m^A are all proportional to E_0^2 , that is, the effects of the energy shifts and ionization pathway are both enhanced with the laser intensity increasing.

Finally, the pulse duration dependence of the frequency ω_m^A revealed in TDSE results is also reproduced by the minimal three-state model. As is shown in Figs. 4(c) and 4(d), the frequency ω_m^A approaches 0.375 a.u. with the increase of the pulse duration. This type of behavior is supported by the TDSE simulations (Fig. 2). To explain this, we inspect the laser pulses in the frequency domain. The spectrum of the laser field in the frequency domain becomes sharper as the pulse duration becomes longer. So, a much smaller blue-shift of the frequency could lead to a significant increase in the ionization rates. Consequently, the required blue-shift for the symmetric doublets decreases with increasing pulse duration.

B. Angular distributions for the AT doublets in PEMDs

Figure 5(a) shows the PEMD obtained from TDSE. The laser frequency, intensity, and pulse duration are $\omega = 0.375$ a.u., $I = 1 \times 10^{14}$ W/cm², and $N = 60$, respectively. Two rings appear in the PEMD and their angular distributions are different. The node of the four-lobe structure for the outer ring is much less visible than that of the inner ring. This is different from the previous study at the relatively low laser intensity where the angular distributions of the doublets are almost the same [57]. The photoelectron angular distribution

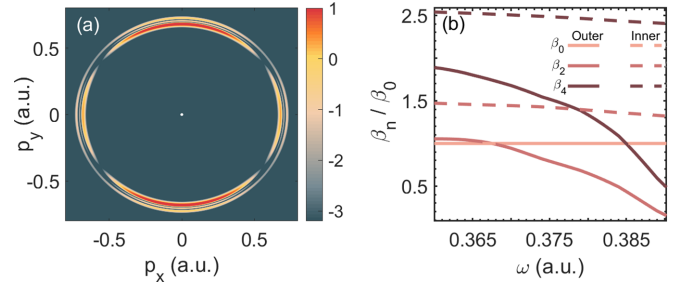


FIG. 5. (a) The PEMD in the polarization plane with the laser frequency $\omega = 0.375$ a.u. The laser intensity is 1×10^{14} W/cm² and the pulse duration is $N = 60$. (b) The asymmetry parameters β_n of PEMDs as a function of the laser frequency. Dashed lines represent the asymmetry parameters β_n of the inner ring in the PEMDs and solid lines represent β_n of the outer ring. The asymmetry parameters β_0 of the inner and outer rings overlap.

can be described by

$$I(\theta) = |A_s Y_{00}(\theta, \varphi) + A_d Y_{20}(\theta, \varphi)|^2 = \beta_0 P_0(\theta) + \beta_2 P_2(\theta) + \beta_4 P_4(\theta), \quad (15)$$

where P_n are the Legendre polynomials, φ is the azimuthal angle, and θ is the angle between the laser polarization and the electron velocity vector. β_n are the asymmetry parameters [47,58], which are written as

$$\begin{aligned} \beta_0 &= \frac{1}{4\pi} [|A_s|^2 + |A_d|^2], \\ \beta_2 &= \frac{1}{4\pi} \left[\frac{10}{7} |A_d|^2 + 2\sqrt{5} |A_s| |A_d| \cos(\phi_s - \phi_d) \right] \\ \beta_4 &= \frac{1}{4\pi} \frac{18}{7} |A_d|^2, \end{aligned} \quad (16)$$

with A_s and A_d being the amplitudes of S and D partial waves, ϕ_s and ϕ_d being the phases of S and D partial waves.

The obtained asymmetry parameters β_n as a function of the laser frequency are shown in Fig. 5(b), where the laser intensity and pulse duration are the same as in Fig. 5(a). The dashed and solid lines represent the parameters β_n obtained from the inner and outer rings of doublets in the PEMDs, respectively. For the inner ring, the parameters β_2 and β_4 are always higher than β_0 and change little as laser frequency increases. For the outer ring, however, β_2 and β_4 decrease noticeably and even become lower than β_0 . This indicates that the contribution of the D partial wave keeps dominant for the inner ring, while the contribution of the S partial wave increases for the outer ring as laser frequency increases.

To understand the angular distribution, we return to the four-state model described by Eq. (6). It is possible to redefine the amplitudes a_I and a_ε as $\tilde{a}_I e^{-i\tilde{S}_I(t)t}$ and $\tilde{a}_\varepsilon e^{-i\tilde{S}_\varepsilon(t)t}$ (\tilde{S}_I and \tilde{S}_ε change slowly over time) [35,43]. For the photoelectron with energy near the peak of the doublets, we can simplify the equation into a two-state model

$$\begin{aligned} i\dot{\tilde{a}}_I(t) &= \int d\varepsilon M_{I\varepsilon} \left(\frac{1}{2} E_0 g(t) \right)^2 e^{i\tilde{\delta}_I t} \tilde{a}_\varepsilon(t), \\ i\dot{\tilde{a}}_\varepsilon(t) &= M_{I\varepsilon}^\dagger \left(\frac{1}{2} E_0 g(t) \right)^2 e^{-i\tilde{\delta}_I t} \tilde{a}_I(t). \end{aligned} \quad (17)$$

Here,

$$M_{I\varepsilon} = \sum_m \frac{\langle I|z|m\rangle\langle m|z|\varepsilon\rangle}{E_\varepsilon - E_m - \omega + i\Gamma_m} \quad (18)$$

is the two-photon transition amplitude, where the index m contains both the resonant state $|R\rangle$ and the nonresonant states $|n\rangle$. $\tilde{\delta}_I$ is the energy detuning

$$\tilde{\delta}_I = E_I + \tilde{S}_I(t) - \tilde{S}_\varepsilon(t) - E_\varepsilon + 2\omega, \quad (19)$$

where

$$\begin{aligned} \tilde{S}_I(t) &= S_I(t) + S_{\text{resonant}}(t), \\ \tilde{S}_\varepsilon(t) &= \int d\varepsilon \sum_m \left(D_{\varepsilon m} \frac{1}{2} E_0 g(t) \right)^2 \frac{2(E_\varepsilon - E_m + i\Gamma_m)}{(E_\varepsilon - E_m + i\Gamma_m)^2 - \omega^2}, \end{aligned} \quad (20)$$

are the energy shift of initial state $|I\rangle$ and the ac-stark shift of the continuum state, respectively. $\tilde{S}_I(t)$ contains the contribution of the nonresonant states $S_I(t)$, and the energy splitting induced by the resonant state $S_{\text{resonant}}(t)$. Γ_m is the ionization rate from the state $|m\rangle$. $\tilde{S}_\varepsilon(t)$ approximately equals to $U_p(t)$. Note that Eq. (17) is valid only for $\tilde{\delta}_I \approx 0$.

$$i\dot{a}_I(t) \cong \left[S_I(t) + \left(-\frac{1}{2}[\Delta\omega + (S_I(t) - S_R(t))] - \frac{i}{2}[\Gamma_I(t) + \Gamma_R(t)] \pm \frac{1}{2}\tilde{\Omega}'(t) \right) - \frac{i}{2}\Gamma_I(t) \right] a_I(t), \quad (22)$$

where

$$\tilde{\Omega}'(t) \cong \sqrt{[D_{IR}E_0g(t)]^2 + \left(\Delta\omega + S_I(t) - S_R(t) - \frac{i}{2}[\Gamma_I(t) + \Gamma_R(t)] \right)^2} \quad (23)$$

is the effective Rabi frequency. Comparing with Eq. (11) (i.e., the case without considering the nonresonant ionization pathway), the Rabi frequency here has taken into account the ionization rate of the initial state $|I\rangle$ due to the nonresonant ionization pathway. Equation (22) indicates that

$$\begin{aligned} \tilde{S}_I(t) &= S_I(t) + S_{\text{resonant}}(t) = S_I(t) \\ &+ \left(-\frac{1}{2}[\Delta\omega + (S_I(t) - S_R(t))] \pm \frac{1}{2}\tilde{\Omega}'(t) \right). \end{aligned} \quad (24)$$

So, the shift \tilde{S}_I can be understood as follows. The nonresonant states induce an energy shift S_I . The Rabi oscillations between the shifted initial and the shifted resonant states induce the splitting of $\tilde{\Omega}'(t)$. The detuning is responsible for the further energy shift $-\frac{1}{2}[\Delta\omega + S_I(t) - S_R(t)]$. The sketch of the energy shift and splitting is shown in Fig. 7.

To check the accuracy of Eq. (24), we calculate the two-photon transition amplitudes for the S and D partial waves with Eq. (21) [59]. Here, we neglect the time dependence of $\tilde{S}_\varepsilon(t)$, $S_I(t)$, and $S_R(t)$. This means that $\tilde{S}_\varepsilon(t)$, $S_I(t)$, and $S_R(t)$ are roughly equivalent to $U_{p0} = E_0^2/4\omega^2$, $S_{R0} = 2.6E_0^2$, and $S_{I0} = -0.7E_0^2$, respectively. The obtained results also

Equations (17) and (18) indicate that the angular distribution can be simply understood from the conventional two-photon transition amplitude though Rabi oscillations occur during the two-photon ionization. To check the accuracy of Eq. (18), we separately calculate the two-photon transition amplitudes for the S and D partial waves at the energy E_ε equaling to inner and outer rings of the AT doublets. For the two-photon transition amplitude in Eq. (18), the infinite summation in the radial part is evaluated with the Dalgarno-Lewis method [59]. The obtained ratio between the S and D partial waves as a function of the laser frequency is shown in Fig. 6 (the dashed lines). It agrees well with the TDSE results, both for the inner and the outer rings.

To intuitively understand the distinct angular distribution and its intensity and pulse duration dependence, we rewrite Eq. (18) as ($\tilde{\delta}_I = 0$)

$$M_{I\varepsilon} = \sum_m \frac{\langle I|z|m\rangle\langle m|z|\varepsilon\rangle}{E_I + \tilde{S}_I(t) - \tilde{S}_\varepsilon(t) - E_m + \omega + i\Gamma_m}. \quad (21)$$

It indicates that $M_{I\varepsilon}$ is just the two-photon transition amplitude of the atom but with the initial energy shifted by $\tilde{S}_I(t) - \tilde{S}_\varepsilon(t)$. To reveal the energy shift $\tilde{S}_I(t)$, we redefine the amplitudes a_I and a_R in Eqs. (9)(I) and (II) as $\tilde{a}_I e^{-i(S_I(t) - \frac{i}{2}\Gamma_I(t))t}$ and $\tilde{a}_R e^{-i(S_R(t) - \frac{i}{2}\Gamma_R(t))t}$ to obtain the general solution of $\tilde{a}_I(t)$ from Eqs. (9)(I) and (II) [35,43], and then redefine them back to obtain the expression for $a_I(t)$. Finally, we have

agree well with TDSE results, as shown in Fig. 6 (the dotted lines).

The results above indicate that the angular distributions of the doublets can be understood from the two-photon transition amplitude due to the significant contribution of the nonresonant pathway. In the relatively low laser intensity, the resonant ionization pathway dominates, and thus the angular distribution is determined from the one-photon transition amplitude (from the resonant state to the final state). In the one-photon transition, the relative contribution of the S and D partial waves changes slowly with the final photoelectron energy, and thus the angular distributions of the doublets are almost the same [57]. In the two-photon transition, the relative contribution of the S and D partial waves oscillates quickly with the photoelectron energy (or laser frequency) [47,48,60,61]. Consequently, the angular distributions are different for the two peaks in the doublets. The two-photon transition amplitude should be calculated for the splitted and energy-shifted initial state. The energy splitting and shifting both depend on the laser intensity and pulse duration. Therefore, the angular distributions of the doublets depend on these parameters of the driving laser pulses.

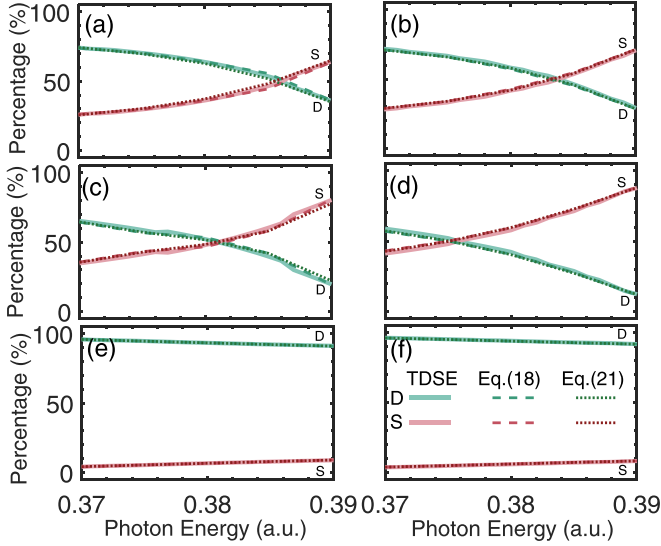


FIG. 6. The percentages of the S (red S lines) and D (green D lines) partial waves as a function of laser frequency. The solid, dashed, and dotted lines represent the results obtained from TDSE, Eq. (18), and Eq. (21), respectively. (a)–(d) The results for the outer ring in PEMDs and (e,f) the results for the inner ring. The pulse durations for the left and right columns are $N = 60$ and 300 , respectively. The laser intensities are 5×10^{13} W/cm² in (a), (b), (e), and (f) and 1×10^{14} W/cm² in (c), (d).

IV. CONCLUSION

We theoretically investigate the TPI of hydrogen atoms in the near-resonant strong-field regime by numerically solving the 3D-TDSE. The PESs show that the asymmetry and the energy spacing of the AT doubles are both affected by the nonresonant states. The effects of the nonresonant states are demonstrated from two aspects. One is the ac-stark shifts of the initial, the resonant, and the continuum states. The other is the nonresonant ionization pathway from the initial state. To identify these two effects, a minimal three-state model containing all the nonresonant states is developed. We find that the laser frequency ω_m^w where the minimum energy spacing of AT doublets locates and the laser frequency ω_m^A where the symmetric AT doublets appears are both blue-shifted from the field-free resonant frequency of 0.375 a.u. The shift of the

frequency ω_m^w is due to the ac-stark shifts of the initial and the resonant states. The shift of the frequency ω_m^A is attributed to both the ac-stark shifts of the initial, the resonant and the continuum states and the contribution of the nonresonant ionization pathway. Furthermore, the shifts of frequencies ω_m^A and ω_m^w increase with the laser intensity because the effects of the energy shifts and nonresonant ionization pathway are both enhanced with the increasing laser intensity.

The PADs are also affected by the nonresonant states. Owing to the nonresonant ionization pathway, the PADs for the lower- and higher-energy peaks in the AT doublets are significantly different. The angular distribution can be described with the conventional two-photon transition amplitude with the energy shifting and splitting of the initial (final) state being considered.

Studying the effect of nonresonant states in near-resonant TPI of more complicated multielectronic target are natural extensions of our work. As long as the two-photon transition amplitude from the initial state via the nonresonant states is comparable with the one-photon transition amplitude from the resonant state, the effects of the nonresonant states could always survive. Inspecting how electron correlation affect the role of the nonresonant states in multielectronic atomic target [40,46,47,62–65], and how electron correlation and nuclear motion affect the role of the nonresonant states in molecular target [66–68] is an intriguing subject which is yet to be explored.

ACKNOWLEDGMENTS

This work was supported by the National Key Research and Development Program of China (Grant No. 2019YFA0308300), the National Natural Science Foundation of China (Grant No. 11874163). A. Csehi is grateful for the support of the János Bolyai Research Scholarship (BO/00474/22/11) of the Hungarian Academy of Sciences and the UNKP-22-5 New National Excellence Program of the Ministry for Culture and Innovation from the source of the National Research, Development, and Innovation Fund. The computing work in this paper is supported by the Public Service Platform of High Performance Computing provided by Network and Computing Center of Huazhong University of Science and Technology (HUST).

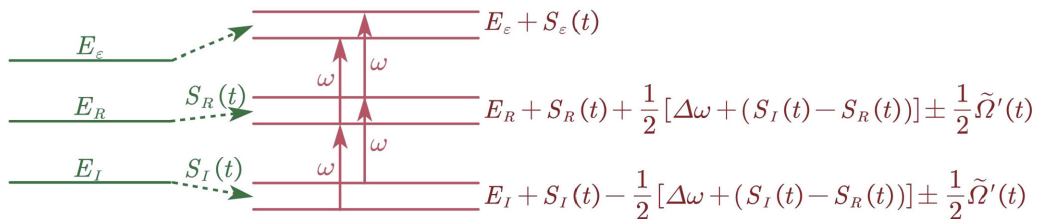


FIG. 7. The sketch of the energy shift and the splitting in the near-resonant laser field. The ac-stark shifts $S_R(t)$, $S_I(t)$, $S_e(t)$ as well as the photon energy detuning $\Delta\omega$ affect the splitting and shift of the energy levels.

- [1] W. Ackermann, D. Maschinnenphysik, G. Asova, V. Ayvazyan, A. Azima, N. Baboi, J. Bähr, V. Balandin, B. Beutner, A Brandt, A. Bolzmann, R. Brinkmann, O. Brovko, M. Castellano, P. Castro, L. Catani, E. Chiadroni, S. Choroba, A. Cianchi, and K. Zapfe, Operation of a free-electron laser from the extreme ultraviolet to the water window, *Nat. Photonics* **1**, 336 (2007).
- [2] P. Emma, R. Akre, J. Arthur, R. Bionta, C. Bostedt, J. Bozek, A. Brachmann, P. Bucksbaum, R. Coffee, F.-J. Decker, Y. Ding, D. Dowell, S. Edstrom, A. Fisher, J. Frisch, S. Gilevich, J. Hastings, G. Hays, and P. Hering, First lasing and operation of an Ångstrom-wavelength free-electron laser, *Nat. Photonics* **4**, 641 (2010).
- [3] E. Allaria, P. Cinquegrana, S. Cleva, D. Cocco, M. Cornacchia, P. Craievich, I. Cudin, G. D'Auria, M. Dal Forno, M. Danailov, R. De Monte, G. Ninno, P. Delgiusto, A. Demidovich, S. Di Mitri, B. Diviacco, A. Fabris, R. Fabris, W. Fawley, and M. Zangrando, Highly coherent and stable pulses from the fermi seeded free-electron laser in the extreme ultraviolet, *Nat. Photonics* **6**, 699 (2012).
- [4] D. Gauthier, P. R. Ribič, G. De Ninno, E. Allaria, P. Cinquegrana, M. B. Danailov, A. Demidovich, E. Ferrari, L. Giannessi, B. Mahieu, and G. Penco, Spectrotemporal Shaping of Seeded Free-Electron Laser Pulses, *Phys. Rev. Lett.* **115**, 114801 (2015).
- [5] N. Miyamoto, M. Kamei, D. Yoshitomi, T. Kanai, T. Sekikawa, T. Nakajima, and S. Watanabe, Observation of Two-Photon Above-Threshold Ionization of Rare Gases by xuv Harmonic Photons, *Phys. Rev. Lett.* **93**, 083903 (2004).
- [6] H. Hasegawa, E. J. Takahashi, Y. Nabekawa, K. L. Ishikawa, and K. Midorikawa, Multiphoton ionization of He by using intense high-order harmonics in the soft-x-ray region, *Phys. Rev. A* **71**, 023407 (2005).
- [7] M. Kretschmar, A. Hadjipittas, B. Major, J. Tümmler, I. Will, T. Nagy, M. J. J. Vrakking, A. Emmanouilidou, and B. Schütte, Attosecond investigation of extreme-ultraviolet multi-photon multi-electron ionization, *Optica* **9**, 639 (2022).
- [8] I. I. Rabi, Space quantization in a gyrating magnetic field, *Phys. Rev.* **51**, 652 (1937).
- [9] B. R. Mollow, Power spectrum of light scattered by two-level systems, *Phys. Rev.* **188**, 1969 (1969).
- [10] P. L. Knight and P. W. Milonni, The rabi frequency in optical spectra, *Phys. Rep.* **66**, 21 (1980).
- [11] A. F. Linskens, I. Holleman, N. Dam, and J. Reuss, Two-photon rabi oscillations, *Phys. Rev. A* **54**, 4854 (1996).
- [12] M. Ruggenthaler and D. Bauer, Rabi Oscillations and Few-Level Approximations in Time-Dependent Density Functional Theory, *Phys. Rev. Lett.* **102**, 233001 (2009).
- [13] K. Nasiri Avanki, D. A. Telnov, and S.-I. Chu, Harmonic generation of li atoms in one- and two-photon rabi-flopping regimes, *Phys. Rev. A* **94**, 053410 (2016).
- [14] V. Stooß, S. M. Cavaletto, S. Donsa, A. Blättermann, P. Birk, C. H. Keitel, I. Březinová, J. Burgdörfer, C. Ott, and T. Pfeifer, Real-Time Reconstruction of the Strong-Field-Driven Dipole Response, *Phys. Rev. Lett.* **121**, 173005 (2018).
- [15] D. A. Tumakov, D. A. Telnov, G. Plunien, and V. M. Shabaev, Photoelectron spectra after multiphoton ionization of li atoms in the one-photon rabi-flopping regime, *Phys. Rev. A* **100**, 023407 (2019).
- [16] A. Magunia, L. Aufleger, T. Ding, P. Rupprecht, M. Rebholz, C. Ott, and T. Pfeifer, Bound-state electron dynamics driven by near-resonantly detuned intense and ultrashort pulsed xuv fields, *Appl. Sci.* **10**, 6153 (2020).
- [17] W. Li, Y. Lei, X. Li, T. Yang, M. Du, Y. Jiang, J. Li, A. Liu, L. He, P. Ma *et al.*, New source for tuning the effective rabi frequency discovered in multiphoton ionization, [arXiv:2112.13096](https://arxiv.org/abs/2112.13096).
- [18] S. H. Autler and C. H. Townes, Stark effect in rapidly varying fields, *Phys. Rev.* **100**, 703 (1955).
- [19] B. Walker, M. Kaluža, B. Sheehy, P. Agostini, and L. F. DiMauro, Observation of Continuum-Continuum Autler-Townes Splitting, *Phys. Rev. Lett.* **75**, 633 (1995).
- [20] J. Qi, G. Lazarov, X. Wang, L. Li, L. M. Narducci, A. M. Lyyra, and F. C. Spano, Autler-Townes Splitting in Molecular Lithium: Prospects for All-Optical Alignment of Nonpolar Molecules, *Phys. Rev. Lett.* **83**, 288 (1999).
- [21] E. H. Ahmed, S. Ingram, T. Kirova, O. Salihoglu, J. Huenekens, J. Qi, Y. Guan, and A. M. Lyyra, Quantum Control of the Spin-Orbit Interaction Using the Autler-Townes Effect, *Phys. Rev. Lett.* **107**, 163601 (2011).
- [22] M. G. Bustamante, V. D. Rodríguez, and R. O. Barrachina, Secondary peaks in the atomic ionization by a resonant laser pulse, *J. Phys.: Conf. Ser.* **397**, 012014 (2012).
- [23] W.-C. Jiang, H. Liang, S. Wang, L.-Y. Peng, and J. Burgdörfer, Enhancing autler-townes splittings by ultrafast xuv pulses, *Phys. Rev. Res.* **3**, L032052 (2021).
- [24] E. P. Kanter, B. Krässig, Y. Li, A. M. March, P. Ho, N. Rohringer, R. Santra, S. H. Southworth, L. F. DiMauro, G. Doumy, C. A. Roedig, N. Berrah, L. Fang, M. Hoener, P. H. Bucksbaum, S. Ghimire, D. A. Reis, J. D. Bozek, C. Bostedt, M. Messerschmidt *et al.*, Unveiling and Driving Hidden Resonances with High-Fluence, High-Intensity X-Ray Pulses, *Phys. Rev. Lett.* **107**, 233001 (2011).
- [25] T. Sako, J. Adachi, A. Yagishita, M. Yabashi, T. Tanaka, M. Nagasono, and T. Ishikawa, Suppression of ionization probability due to Rabi oscillations in the resonance two-photon ionization of he by euv free-electron lasers, *Phys. Rev. A* **84**, 053419 (2011).
- [26] M. Fushitani, C. Liu, A. Matsuda, T. Endo, Y. Toida, M. Nagasono, T. Togashi, M. Yabashi, T. Ishikawa, Y. Hikosaka, T. Morishita, and A. Hishikawa, Femtosecond two-photon rabi oscillations in excited he driven by ultrashort intense laser fields, *Nat. Photonics* **10**, 102 (2015).
- [27] J. H. Shirley, Solution of the schrödinger equation with a Hamiltonian periodic in time, *Phys. Rev.* **138**, B979 (1965).
- [28] S. R. Barone, M. A. Narcowich, and F. J. Narcowich, Floquet theory and applications, *Phys. Rev. A* **15**, 1109 (1977).
- [29] M. S. Rudner and N. H. Lindner, The floquet engineer's handbook, [arXiv:2003.08252v2](https://arxiv.org/abs/2003.08252v2).
- [30] K. Toyota, O. I. Tolstikhin, T. Morishita, and S. Watanabe, Siegert-state expansion in the kramers-henneberger frame: Interference substructure of above-threshold ionization peaks in the stabilization regime, *Phys. Rev. A* **76**, 043418 (2007).
- [31] K. Toyota, O. I. Tolstikhin, T. Morishita, and S. Watanabe, Interference substructure of above-threshold ionization peaks in the stabilization regime, *Phys. Rev. A* **78**, 033432 (2008).
- [32] K. Toyota, U. Saalman, and J. M. Rost, The envelope hamiltonian for electron interaction with ultrashort pulses, *New J. Phys.* **17**, 073005 (2015).

- [33] R. R. Jones, Interference Effects in the Multiphoton Ionization of Sodium, *Phys. Rev. Lett.* **74**, 1091 (1995).
- [34] O. I. Tolstikhin, Siegert-state expansion for nonstationary systems. iv. three-dimensional case, *Phys. Rev. A* **77**, 032712 (2008).
- [35] P. V. Demekhin and L. S. Cederbaum, Strong interference effects in the resonant Auger decay of atoms induced by intense x-ray fields, *Phys. Rev. A* **83**, 023422 (2011).
- [36] P. V. Demekhin and L. S. Cederbaum, Coherent intense resonant laser pulses lead to interference in the time domain seen in the spectrum of the emitted particles, *Phys. Rev. A* **86**, 063412 (2012).
- [37] P. V. Demekhin and L. S. Cederbaum, Dynamic Interference of Photoelectrons Produced by High-Frequency Laser Pulses, *Phys. Rev. Lett.* **108**, 253001 (2012).
- [38] P. V. Demekhin and L. S. Cederbaum, ac stark effect in the electronic continuum and its impact on the photoionization of atoms by coherent intense short high-frequency laser pulses, *Phys. Rev. A* **88**, 043414 (2013).
- [39] S. B. Zhang and N. Rohringer, Photoemission spectroscopy with high-intensity short-wavelength lasers, *Phys. Rev. A* **89**, 013407 (2014).
- [40] A. N. Artemyev, A. D. Müller, D. Hochstuhl, L. S. Cederbaum, and P. V. Demekhin, Dynamic interference in the photoionization of He by coherent intense high-frequency laser pulses: Direct propagation of the two-electron wave packets on large spatial grids, *Phys. Rev. A* **93**, 043418 (2016).
- [41] M. Bagheri, U. Saalmann, and J. M. Rost, Essential Conditions for Dynamic Interference, *Phys. Rev. Lett.* **118**, 143202 (2017).
- [42] W.-C. Jiang and J. Burgdörfer, Dynamic interference as signature of atomic stabilization, *Opt. Express* **26**, 19921 (2018).
- [43] A. Tóth and A. Csehi, Probing strong-field two-photon transitions through dynamic interference, *J. Phys. B: At., Mol. Opt. Phys.* **54**, 035005 (2021).
- [44] T. Sato, A. Iwasaki, K. Ishibashi, T. Okino, K. Yamanouchi, J. Adachi, A. Yagishita, H. Yazawa, F. Kannari, M. Aoyama, K. Yamakawa, K. Midorikawa, H. Nakano, M. Yabashi, M. Nagasono, A. Higashiya, and T. Ishikawa, Determination of the absolute two-photon ionization cross section of He by an XUV free electron laser, *J. Phys. B: At., Mol. Opt. Phys.* **44**, 161001 (2011).
- [45] N. Miyauchi, Jun-ichi Adachi, A. Yagishita, T. Sako, F. Koike, T. Sato, A. Iwasaki, T. Okino, K. Yamanouchi, K. Midorikawa, K. Yamakawa, F. Kannari, H. Nakano, M. Nagasono, K. Tono, M. Yabashi, T. Ishikawa, T. Togashi, H. Ohashi, and Y. Senba, Three-photon double ionization of Ar studied by photoelectron spectroscopy using an extreme ultraviolet free-electron laser: Manifestation of resonance states of an intermediate Ar^+ ion, *J. Phys. B: At., Mol. Opt. Phys.* **44**, 071001 (2011).
- [46] B. Kaiser, A. Brand, M. Glässl, A. Vagov, V. M. Axt, and U. Pietsch, Photoionization of resonantly driven atomic states by an extreme ultraviolet-free-electron laser: Intensity dependence and renormalization of Rabi frequencies, *New J. Phys.* **15**, 093016 (2013).
- [47] K. L. Ishikawa and K. Ueda, Competition of Resonant and Nonresonant Paths in Resonance-Enhanced Two-Photon Single Ionization of He by an Ultrashort Extreme-Ultraviolet Pulse, *Phys. Rev. Lett.* **108**, 033003 (2012).
- [48] M.-X. Wang, H. Liang, X.-R. Xiao, S.-G. Chen, and L.-Y. Peng, Time-dependent perturbation theory beyond the dipole approximation for two-photon ionization of atoms, *Phys. Rev. A* **99**, 023407 (2019).
- [49] S. Nandi, E. Olofsson, M. Bertolino, S. Carlström, F. Zapata, D. Busto, C. Callegari, M. Di Fraia, P. Eng-Johnsson, R. Feifel *et al.*, Observation of Rabi dynamics with a short-wavelength free-electron laser, *Nature (London)* **608**, 488 (2022).
- [50] T. N. Rescigno and C. W. McCurdy, Numerical grid methods for quantum-mechanical scattering problems, *Phys. Rev. A* **62**, 032706 (2000).
- [51] W.-C. Jiang and X. Tian, Efficient split-lanczos propagator for strong-field ionization of atoms, *Opt. Express* **25**, 26832 (2017).
- [52] D. G. Arbó, J. E. Miraglia, M. S. Gravielle, K. Schiessl, E. Persson, and J. Burgdörfer, Coulomb-volkov approximation for near-threshold ionization by short laser pulses, *Phys. Rev. A* **77**, 013401 (2008).
- [53] B. Kaufman, T. Rozgonyi, P. Marquetand, and T. Weinacht, Adiabatic elimination in strong-field light-matter coupling, *Phys. Rev. A* **102**, 063117 (2020).
- [54] B. W. Shore, *Manipulating Quantum Structures Using Laser Pulses* (Cambridge University Press, Cambridge, England, 2011).
- [55] L. S. Cederbaum and W. Domcke, Local against non-local complex potential in resonant electron-molecule scattering, *J. Phys. B* **14**, 4665 (1981).
- [56] W. Domcke, Theory of resonance and threshold effects in electron-molecule collisions: The projection-operator approach, *Phys. Rep.* **208**, 97 (1991).
- [57] A. D. Müller, E. Kutscher, A. N. Artemyev, L. S. Cederbaum, and P. V. Demekhin, Dynamic interference in the resonance-enhanced multiphoton ionization of hydrogen atoms by short and intense laser pulses, *Chem. Phys.* **509**, 145 (2018).
- [58] S. J. Smith and G. Leuchs, Angular correlation in multiphoton ionization of atoms, *Adv. At. Mol. Phys.* **24**, 157 (1988).
- [59] A. Dalgarno, J. T. Lewis, and D. R. Bates, The exact calculation of long-range forces between atoms by perturbation theory, *Proc. R. Soc. London A* **233**, 70 (1955).
- [60] M.-X. Wang, X.-R. Xiao, H. Liang, S.-G. Chen, and L.-Y. Peng, Photon-momentum transfer in one- and two-photon ionization of atoms, *Phys. Rev. A* **96**, 043414 (2017).
- [61] D. Busto, J. Vinbladh, S. Zhong, M. Isinger, S. Nandi, S. Maclot, P. Johnsson, M. Gisselbrecht, A. L'Huillier, E. Lindroth, and J. M. Dahlström, Fano's Propensity Rule in Angle-Resolved Attosecond Pump-Probe Photoionization, *Phys. Rev. Lett.* **123**, 133201 (2019).
- [62] R. Moshhammer, Y. H. Jiang, L. Foucar, A. Rudenko, Th. Ergler, C. D. Schröter, S. Lüdemann, K. Zrost, D. Fischer, J. Titze, T. Jahnke, M. Schöffler, T. Weber, R. Dörner, T. J. M. Zouros, A. Dorn, T. Ferger, K. U. Kühnel, S. Düsterer, R. Treusch *et al.*, Few-Photon Multiple Ionization of Ne and Ar by Strong Free-Electron-Laser Pulses, *Phys. Rev. Lett.* **98**, 203001 (2007).
- [63] Q. Liao, Y. Zhou, C. Huang, and P. Lu, Multiphoton Rabi oscillations of correlated electrons in strong-field nonsequential double ionization, *New J. Phys.* **14**, 013001 (2012).
- [64] M. Flögel, J. Durá, B. Schütte, M. Ivanov, A. Rouzée, and M. J. J. Vrakking, Rabi oscillations in extreme ultraviolet ionization of atomic argon, *Phys. Rev. A* **95**, 021401(R) (2017).
- [65] Y. Chen, Y. Zhou, Y. Li, M. Li, P. Lan, and P. Lu, Rabi oscillation in few-photon double ionization through doubly excited states, *Phys. Rev. A* **97**, 013428 (2018).

- [66] S. X. Hu, W. X. Qu, and Z. Z. Xu, Electron-correlation effects in intense-field ionization of hydrogen molecules, *Phys. Rev. A* **57**, 3770 (1998).
- [67] A. Palacios, H. Bachau, and F. Martín, Step-ladder rabi oscillations in molecules exposed to intense ultrashort vuv pulses, *Phys. Rev. A* **74**, 031402(R) (2006).
- [68] F. Holzmeier, R. Y. Bello, M. Hervé, A. Achner, T. M. Baumann, M. Meyer, P. Finetti, M. Di Fraia, D. Gauthier, E. Roussel, O. Plekan, R. Richter, K. C. Prince, C. Callegari, H. Bachau, A. Palacios, F. Martín, and D. Doweck, Control of h_2 Dissociative Ionization in the Nonlinear Regime Using Vacuum Ultraviolet Free-Electron Laser Pulses, *Phys. Rev. Lett.* **121**, 103002 (2018).